ADVANCED ENERGY MATERIALS
www.advenergymat.de

Robust Thin Films-Based Triboelectric Nanogenerator Arrays for Harvesting Bidirectional Wind Energy

*Zuci Quan, Chang Bao Han, Tao Jiang, and Zhong Lin Wang**

Wind-driven triboelectric nanogenerators (TENGs) play an important role in harvesting energy from ambient environments. Compared to single-side-fixed triboelectric nanogenerator (STENG) arrays for harvesting single-pathway wind energy, double-side-fixed triboelectric nanogenerator (DTENG) arrays are developed to harvest bidirectional wind energy. Electrical performances of the STENG and DTENG can be improved due to sticky, abrasive, and electrical properties of the Ti buffer layers among Al, polytetrafluoroethylene (PTFE), and polyimide (Kapton), configuring in triboelectric PTFE/Ti/Al and Al/Ti/Kapton/Ti/Al thin films. Short-circuit current (I_{SC}), open-circuit voltage (V_{OC}), and frequencies of the STENG and DTENG increase with increasing wind velocity ranging from 9.2 to 18.4 m s^{-1}, revealing that the moderate I_{SC}, V_{OC}, frequencies, and output powers of the STENG and DTENG reach 67 μA, 57 μA, 334 V, 296 V, 173 Hz, 162 Hz, 5.5 mW and 3.4 mW with a matched load of 4 MΩ at airflow rate of 15.9 m s^{-1}, respectively. Compared with counterparts of the single-pathway-harvested STENG arrays, the I_{SC}, durability, and stability of the bidirectional-harvested DTENG can be dramatically improved by a 4 × 1 array connected in parallel because of the improved device configuration, stickiness, and abrasion by adhering Ti buffer layers. The durable DTENG arrays present a step toward practical applications in harvesting bidirectional wind energy for self-powered systems and wireless sensors.

1. Introduction

Energy harvesting is an adaptable, reliable, sustainable, eco-friendly, and cost-efficient technique to convert diverse environmental energies to useful electrical energy.[1,2] Energy harvesting from wind, ultrasonic wave, mechanical vibration, thermal, pyroelectric transportation, chemical, light, photonic systems, electromagnetic radiation, medical applications and so on, is a key question for the sustainable development of our society.[3–15] Technologies to harvest electrical energy from wind have extensive applications in self-powered systems of wireless electronics, mobile electronics, wearable electronics, civil engineering, and national security because wind energy is one of the cleanest, most abundant, sustainable, and cost-efficient energies based on the threat of global warming and energy crisis.[4–18] Some previous researches in nanogenerators were focused on piezoelectric materials, including ZnO, GaN, InN, MoS_2, polyvinylidene fluoride, lead zirconium titanate, $BaTiO_3$, $BiFeO_3$, $NaNbO_3$, $(1-x)Pb(Mg_{1/3}Nb_{2/3})O_3$-$xPbTiO_3$, $0.9525K_{0.5}Na_{0.5}NbO_3$-$0.0475LiTaO_3$, and triangular-belt $ZnSnO_3$, where a deformation of the piezoelectric material converted a small-scale mechanical energy into electricity.[18–28] Recently, triboelectric nanogenerators (TENGs) based on the coupling between triboelectrification and electrostatic induction have been developed as a novel means of harvesting energy due to the unprecedented advantages of simple fabrication, light weight, excellent reliability, low cost, high power density, high energy conversion efficiency, and abundant choices of materials since 2012.[13–17]

In particular, wind-induced TENG with fluttering membranes has been suggested as an alternative to overcome the drawbacks of wind-turbine-based wind energy generator including structural complexity, the large volume and weight, high cost of manufacturing and installation, low efficiency and noise.[3] Bae et al. demonstrated that there had been considerable research on the basic dynamics of flexible structures like flags, which could be bent, folded, twisted, or waved.[3,29] It was reported that the flutter-driven TENG having small dimensions of 75 mm × 50 mm exhibited the electrical performances: an instantaneous output voltage of 200 V, a current of 60 μA with a frequency of 158 Hz, and an average power of about 0.86 mW at the airflow rate of 15 m s^{-1}.[3] Meng et al. reported that the airflow-driven TENG with the size of 90 mm × 50 mm × 15 mm consisted of an undulating polyimide (Kapton) film and nine-unit-segmented Al electrodes on the single substrate, revealing the maximum open-circuit voltage (V_{OC}) of 30 V at 103 Hz without segmentation, a rectified short-circuit current (I_{SC}) of

Dr. Z. C. Quan, Dr. C. B. Han, Dr. T. Jiang, Prof. Z. L. Wang
Beijing Institute of Nanoenergy and Nanosystems
Chinese Academy of Sciences
Beijing 100083, P. R. China
E-mail: zlwang@gatech.edu
Dr. Z. C. Quan
Department of Physics
Nanchang University
Nanchang 330031, P. R. China
Prof. Z. L. Wang
School of Materials Science and Engineering
Georgia Institute of Technology
Atlanta, GA 30332-0245, USA

DOI: 10.1002/aenm.201501799

about 5 μA after segmenting, and an average output power of 0.035 mW at the matched load of 60 MΩ, which could directly light up 40 commercial light-emitting diodes (LEDs) at wind velocity of 12.6 m s^{-1}.[30] As toward the further applications, three essential issues need to be addressed for the wind-driven TENGs. First, the TENG array needs to work under the airflow condition, which requires the special design for the device structures and materials in consideration of wind direction. Second, the electric energy produced by the wind-driven TENG arrays can be enough to directly power some mobile electronic devices and wireless sensors. Third, since the triboelectrification is a result of two materials in physical contact, the durability and stability of the wind-driven TENG arrays need to be continuously improved.

In this work, we comparatively present single-side-fixed triboelectric nanogenerator (STENG) and double-side-fixed triboelectric nanogenerator (DTENG) arrays. Working mechanism of both STENG and DTENG is based on the coupling of triboelectrification and electrostatic induction between top and/or bottom polytetrafluoroethylene (PTFE) and the undulating Al/Ti/Kapton/Ti/Al thin films. The I_{SC}, V_{OC}, and frequencies of the STENG and DTENG increase with increasing wind velocity in the range from 9.2 to 18.4 m s^{-1}. The maximum I_{SC}, V_{OC}, and frequencies of the STENG and DTENG reach 75 μA, 66 μA, 396 V, 342 V, 186 Hz, and 178 Hz at wind speed of 18.4 m s^{-1}, respectively. The maximum output powers of the STENG and DTENG are 5.5 mW and 3.4 mW at a matched load of 4 MΩ with airflow rate of 15.9 m s^{-1}. To get a visualization of the wind-fluttered DTENG powering external load, a liquid crystal display (LCD) is driven by the DTENG at wind velocity of 1.5 m s^{-1} (see Movie S1, Supporting Information). Compared with counterparts of the 1 × 1, 2 × 1, 2 × 2, and 4 × 1 STENG arrays connected in parallel, the I_{SC} value of the bidirectional 4 × 1 DTENG array is 98 μA, which is degraded to 3.1% after wind blows for 240 min at velocity of 15.9 m s^{-1}, implying that durability and stability of the bidirectional DTENG arrays can be observably improved in comparison with those of the single-pathway-harvested STENG arrays. The DTENG arrays have potential applications in harvesting bidirectional wind energy for self-powered systems and wireless sensors.

2. Results and Discussion

2.1. Schematic Diagrams of STENG and DTENG Arrays

Figure 1 illustrates typical sketches of the 1 × 1, 2 × 2, and 4 × 1 STENG and DTENG arrays. One side of the Al/Ti/Kapton/Ti/Al film for single STENG was fixed in the middle of the acrylic tube, leaving the other side free-standing, as schematically illustrated in Figure 1a. Figure 1b describes that two sides of the Al/Ti/Kapton/Ti/Al film for the DTENG were fixed in the middle of the acrylic tube. Figure 1c,d illustrates sketches of 2 × 2 and 4 × 1 DTENG arrays connected in parallel by copper wires in the electrical circuit board. Both the STENG and DTENG devices consist of the top and bottom PTFE/Ti/Al patches and the vibrational Al/Ti/Kapton/Ti/Al film, where the sputtered Al/Ti thin films deposited on both sides of Kapton film play three roles: (1) the upper and lower triboelectric surfaces; (2) Al/Ti bilayer electrodes by adhering Ti buffer layer, resulting in two TENGs in single device (namely, TENG1 and TENG2 as described in Figure S1, Supporting Information); and (3) transportation of wave energy when the Al/Ti/Kapton/Ti/Al thin films are fluttered at the appropriate wind velocity.

2.2. Working Mechanism of the STENG and DTENG

Working mechanism of both the STENG and DTENG is schematically depicted in **Figure 2**a–g step by step. At the original state before the contact of the PTFE film and the Al/Ti electrode, there is no electric output for both TENG1 and TENG2, as displayed in Figure 2a. Once the Al/Ti electrode contacts with the PTFE film, electrons are transferred from Al/Ti into the PTFE film since the PTFE is much more triboelectrically negative than the Al/Ti according to the triboelectric series.[11,13,31] However, no electron flow occurs in the external circuit since the produced tribocharges with opposite polarities are fully balanced, as shown in Figure 2b. The produced negative tribocharges in this process can be preserved on the PTFE surface due to the nature of the insulator. The positive tribocharges on the middle Al can flow through an external load to the top Al, when these tribocharges cannot be compensated according to separation between the top PTFE film and the middle Al/Ti electrode deposited on the Kapton film, as described in Figure 2c. This electrostatic induction process can produce output electrical signals for the TENG1 until the negative tribocharges on the top PTFE film are fully screened from the tribocharges on the middle Al, as illustrated in Figure 2d. At this state, the contact between the middle Al and the bottom PTFE film can produce the positive and negative tribocharges, respectively. When the Al/Ti/Kapton/Ti/Al film moves back from the bottom to the top of the device, the electron flow occurs from the bottom Al to the middle Al on the Kapton film for the TENG2, as shown in Figure 2e. The electrons flow from the middle Al to the top Al for TENG1, when the contact between the middle Al and the top PTFE film occurs, as shown in Figure 2f. When the lower Al on the Kapton film moves to the bottom PTFE, the electrons flow from the top Al to the middle Al, as shown in Figure 2g. Therefore, when airflow vibrates the Al/Ti/Kapton/Ti/Al film up and down in the acrylic tube, the TENG1 or TENG2 acts as an electron pump that drives the electrons back and forth between the top and bottom Al due to the electrostatic induction, producing an alternative current in the external circuit.

2.3. Theoretical Simulation via COMSOL

Figure 3a,b presents electric potential distributions of the STENG and DTENG at the representative states. Corresponding V_{OC} values depend on position of wind-entering space in both sides are simulated by COMSOL, meanwhile the maximum V_{OC} of the STENG and DTENG are obtained when the position is 3 mm, as plotted in Figure 3c,d (see the Supporting Information). Figure 3e,f depicts the measured I_{SC} and V_{OC} values of the STENG and DTENG with various positions of wind-entering space. The maximum I_{SC} and V_{OC} values are also obtained when the position of wind-entering space is 3 mm.

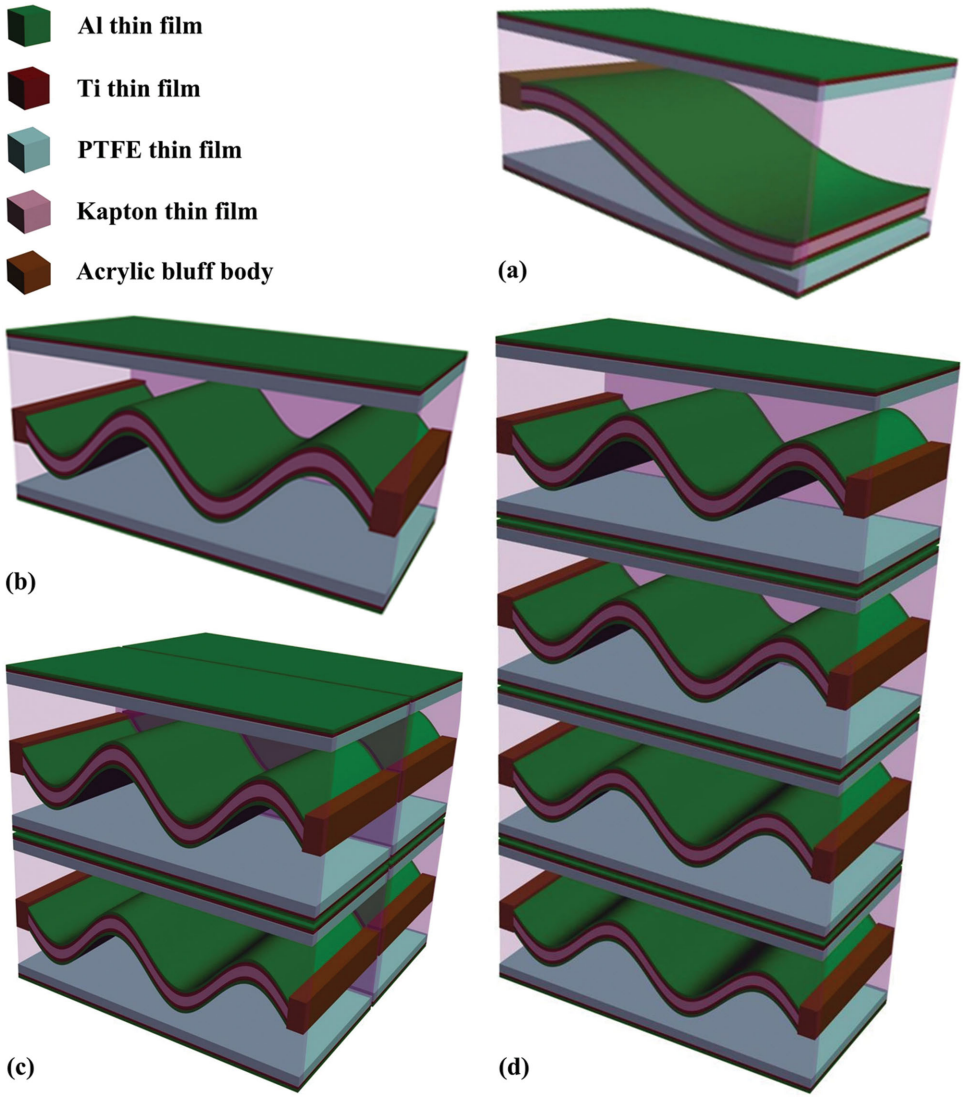

Figure 1. Schematic diagrams of the STENG and DTENG arrays: a) 1 × 1 STENG and b–d) 1 × 1, 2 × 2, and 4 × 1 DTENG arrays.

Experimental results agree with the simulated trends for the position of 3 mm. Figure 3d reveals that the simulated V_{OCS} of the STENG are undulating with an average V_{OCS} value of 369.1 ± 223.9 V. The maximum V_{OCS} value of the STENG reaches 600.3 V when the sandwiched Al/Kapton/Al film locates in the middle of the top and bottom PTFE/Al films, while the minimum V_{OCS} value is 113.5 V when the Al/Kapton/Al film approaches the top or bottom PTFE/Al film due to the electric potential offset between the TENG1 and TENG2, as described in Figure 2. Compared to the undulating V_{OCS} values of the STENG, the potential difference (V_{OCD}) values of the DTENG with an average V_{OCD} value of 507.1 ± 40.5 V are relatively stable according to synergetic roles of the fluttered Al/Kapton/Al film, the elastic force, the constrained force of double sides and the driving force generated by the DTENG, indicating that the stable V_{OCD} values of the DTENG device are expertly obtained at the appropriate wind velocity, as depicted in Figure 3d. It is noted that these states of the DTENG are typical ones at the appropriate wind velocities, and low V_{OCD} values can be also obtained when the fluttered Al/Kapton/Al states are similar to those shown in Figure 3a3,a5. It can be inferred that variance of the electric potential distributions for the STENG and DTENG serves as the driving force for electron flow.[32,33]

2.4. Output Performances of the STENG and DTENG Arrays

To investigate the I_{SC} and V_{OC} values for both the STENG and DTENG as functions of wind velocities, a systematic measurement was carried out under wind velocities ranging from 9.2 to 18.4 m s^{-1}. As illustrated in **Figure 4**a, the rectified I_{SSF1} values of the STENG1 increase with increasing wind velocity with the maximum value of 54 μA at 18.4 m s^{-1}. As described in Figure 4b, the rectified I_{SSF2} values of the STENG2 also increase with increasing wind velocity and with the maximum value of 46 μA at 18.4 m s^{-1}. To obtain the larger I_{SC} output, the rectified I_{SC} signals of the STENG1 and STENG2 are connected in parallel, namely STENG1 // STENG2 is assigned to I_{SSF3} in

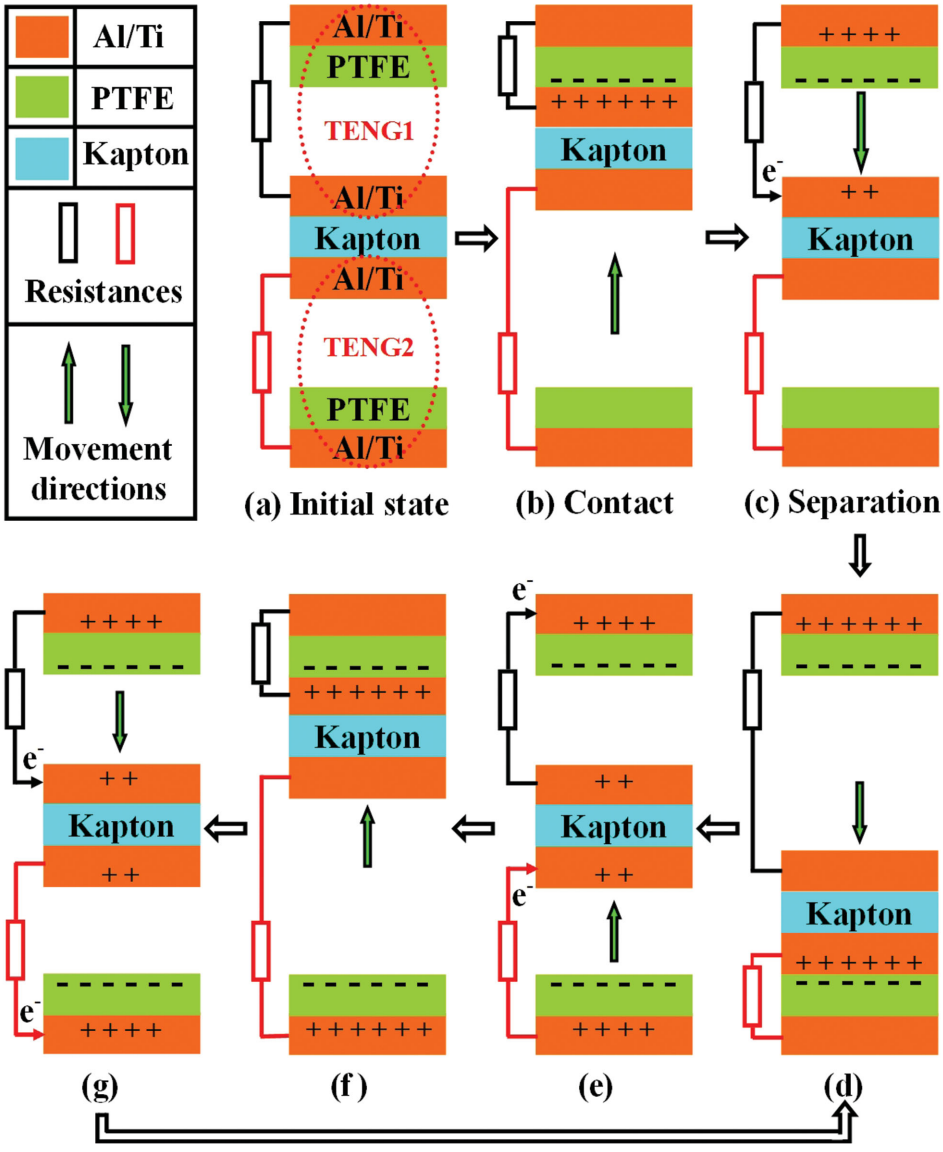

Figure 2. Sketches that illustrate the electricity generation process in full cycle under wind-driven vibration of Al/Ti/Kapton/Ti/Al thin film between two PTFE/Ti/Al thin films adhered on top and bottom of the acrylic tube.

Figure 4c. Compared to the I_{SSF1} and I_{SSF2} for the STENG, the I_{SSF3} values increase slightly with maximum value of 75 μA at 18.4 m s^{-1}. It can be found that there are no obvious enhancements of the I_{SSF3} values in comparison with the I_{SSF1} and I_{SSF2} values of the STENG, which are associated with the asynchronism for the output signals of the STENG1 and STENG2 when wind blows. Similarly, Figure 4d–f shows that the rectified I_{DSF1} for DTENG1, I_{DSF2} for DTENG2 and I_{DSF3} for DTENG1 // DTENG2 also increase with increasing wind velocity in the range from 9.2 to 18.4 m s^{-1}, revealing the corresponding maximum values of 56, 49 and 66 μA, respectively. Compared to the I_{DSF1} and I_{DSF2} values, the I_{DSF3} values also have not obvious enhancements because of the asynchronism for the output signals of the DTENG1 and DTENG2.

Figure 4g presents that the V_{SSF} values of the STENG increase from 167 to 396 V with increasing wind velocity ranging from 9.2 to 18.4 m s^{-1}. Figure 4h illustrates that the V_{DSF} values of the DTENG increase from 140 to 342 V with increasing wind velocity ranging from 9.2 to 18.4 m s^{-1}. It is apparently observed that the absolute values of the negative V_{SSF} and V_{DSF} values are larger than the positive counterparts in amplitude due to the asymmetric fluttering of between the PTFE/Ti/Al film and the middle Al/Ti/Kapton/Ti/Al. These results can be explained by an efficient change in surface contact area in the fluttered movement with increasing wind velocity. At the higher wind velocity, a higher fluttered speed of the Al/Ti/Kapton/Ti/Al film leads to the enhanced contact/separation force. Since the top and bottom PTFE have some nanostructures etched by the $CF_4/Ar/O_2$ plasma, a larger contact force will enhance the nanoscale contact area between the PTFE film and the middle Al/Ti electrodes, resulting in a higher surface charge density.[11,13] It means that the coupling between wind velocity and

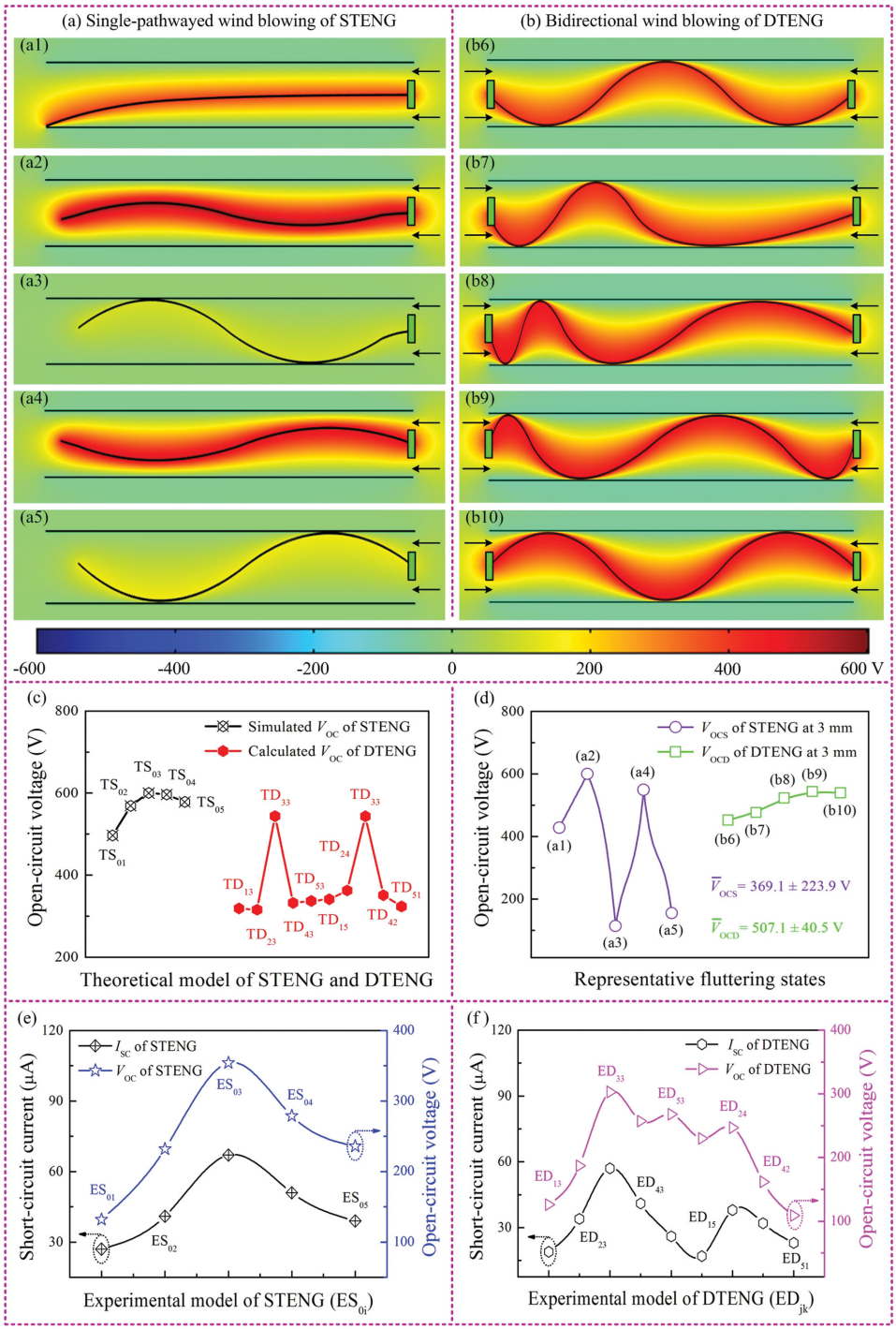

Figure 3. COMSOL simulation of electric potential distributions and potential differences for the STENG and DTENG under an open-circuit condition: a) the STENG fluttered at representative states, b) the DTENG fluttered at certain states, c) the simulated V_{OC} of the STENG (TS_{0i}, where i = 1, 2, 3, 4, 5) and DTENG (TD_{jk}, where j = 1, 2, 3, 4, 5 and k = 1, 2, 3, 4, 5) depend on position of wind-entering space in both sides, and d) the calculated V_{OC} values (V_{OCS} and V_{OCD}) of the STENG and DTENG when the position of wind-entering space is 3 mm. e,f) The measured I_{SC} and V_{OC} values of the STENG and DTENG with various positions of wind-entering space. The maximum I_{SC} and V_{OC} values are obtained when the position of wind-entering space is 3 mm.

fluttered motion may lead to the increased V_{SSF} and V_{DSF} values for the STENG and DTENG devices at a higher wind velocity.

Figure 5a,b illustrates measured circuits of the current and voltage for the STENG and DTENG, respectively. Figure 5c shows the I_{SC} values of the STENG and DTENG with or without Ti buffer layers, implying that the I_{SC} values for the STENG and DTENG increase with increasing wind velocity ranging from 9.2 to 18.4 m s^{-1}, respectively. It is found that I_{SCSP2}

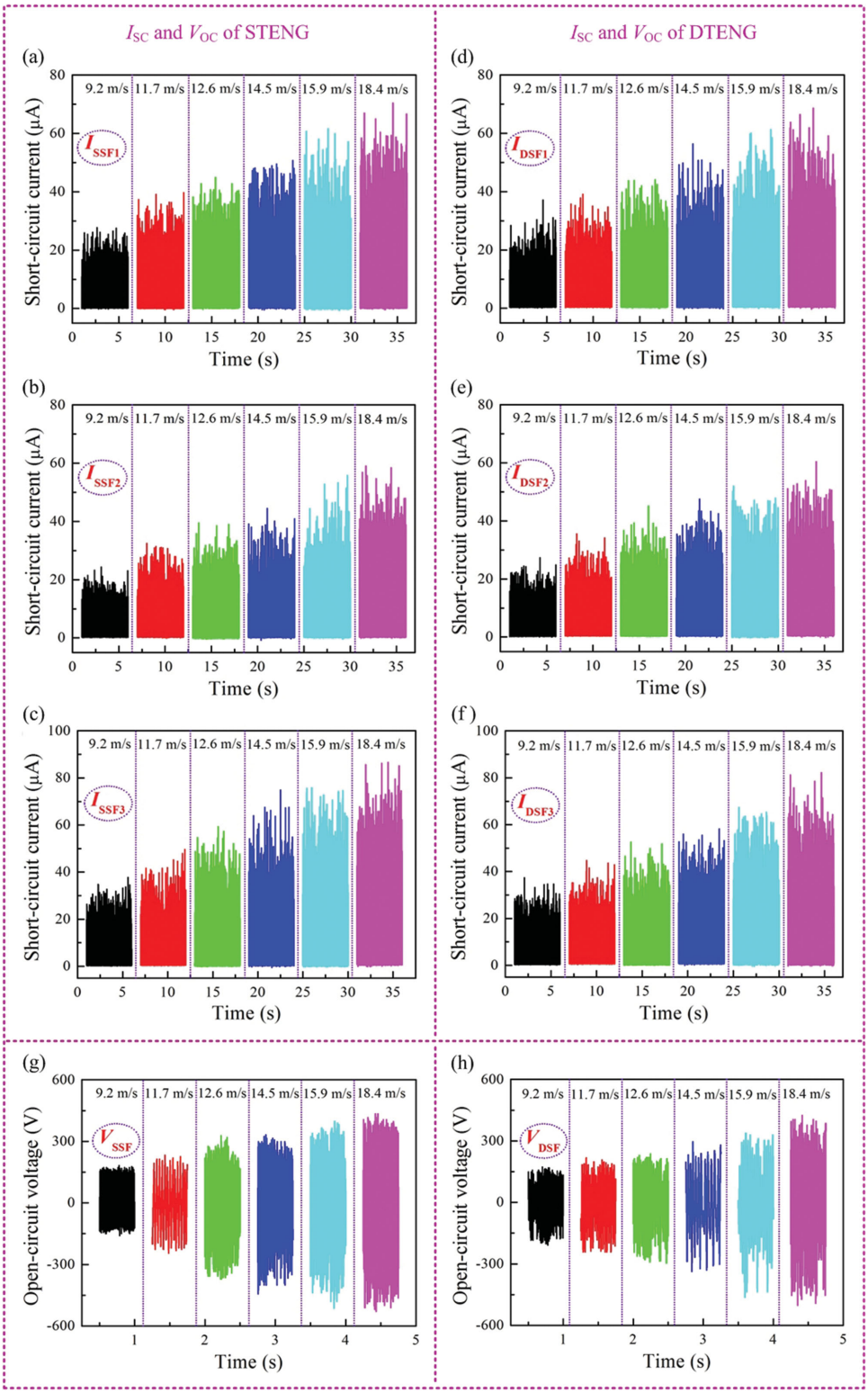

Figure 4. Rectified I_{SC} values of the STENG and DTENG as functions of wind velocities ranging from 9.2 to 18.4 m s^{-1}: a) I_{SSF1} values for the STENG1, b) I_{SSF2} values for the STENG2, c) I_{SSF3} values for the STENG1 and STENG2 connected in parallel, d) I_{DSF1} values for the DTENG1, e) I_{DSF2} values for the DTENG2, and f) I_{DSF3} values for the DTENG1 and DTENG2 connected in parallel. The V_{OC} values of the STENG and DTENG depend on wind velocity, g) V_{SSF} values for the STENG and h) V_{DSF} values for the DTENG.

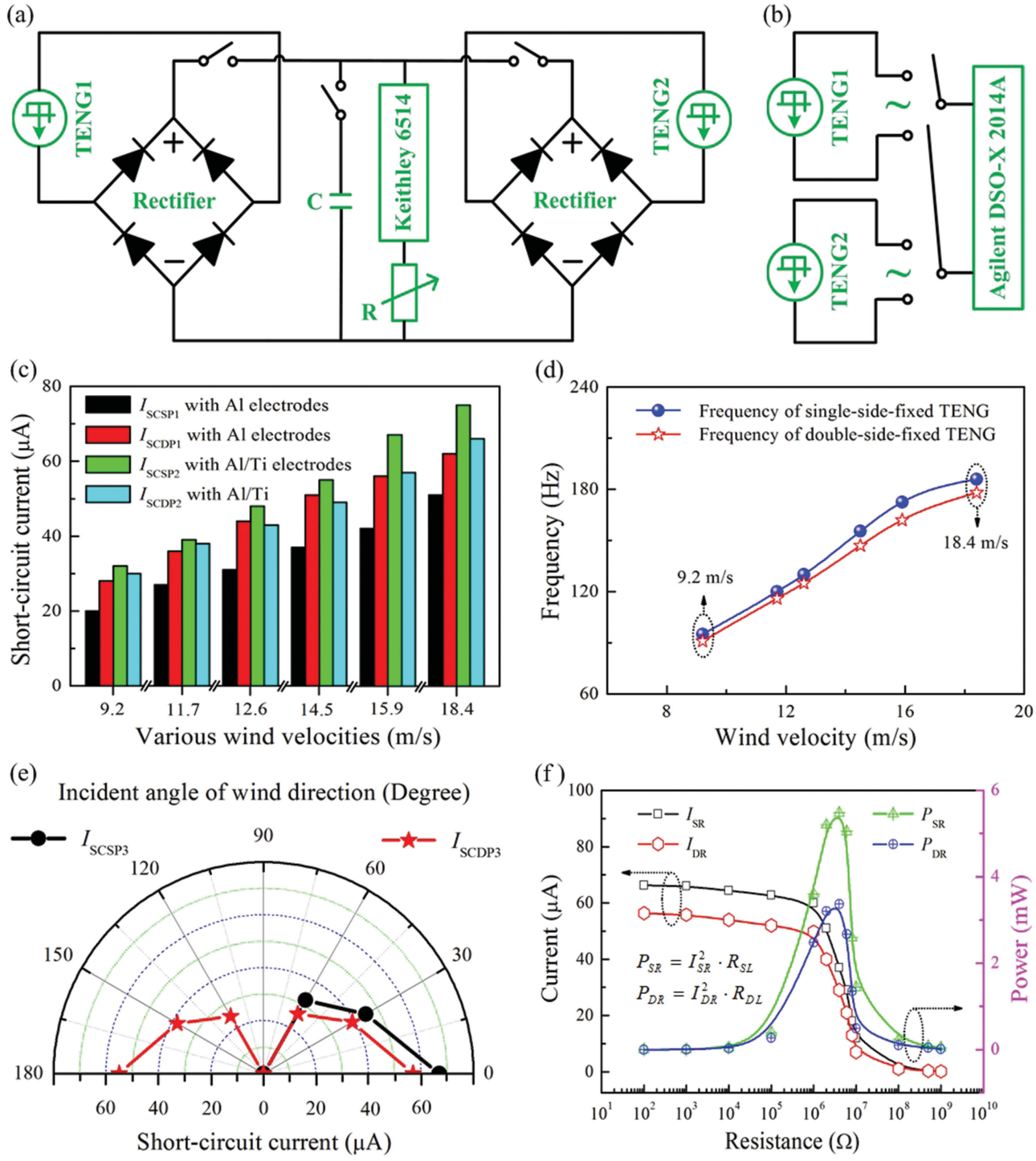

Figure 5. a,b) Measured circuits of current and voltage for the STENG and DTENG. c) Rectified I_{SCSP1}, I_{SCSP2}, I_{SCDP1}, and I_{SCDP2} values of the STENG and DTENG with or without Ti buffer layers depend on wind velocity in the range from 9.2 to 18.4 m s^{-1}, respectively. d) Frequencies of the STENG and DTENG as functions of wind velocity ranging from 9.2 to 18.4 m s^{-1}. e) Rectified I_{SC} values of the STENG (I_{SCSP3}) and DTENG (I_{SCDP3}) depend on incident angle of wind direction in the range from 0° to 180°. f) Output currents (I_{SR} and I_{DR}) and powers (P_{SR} and P_{DR}) of the STENG and DTENG depend on external load in the range from 100 to 10^9 Ω, respectively.

and I_{SCDP2} values of the STENG and DTENG with Ti buffer layers are larger than I_{SCSP1} and I_{SCDP1} values of the devices without Ti buffer layers. It is the reason that a higher wind speed results in both more transferred charges as discussed before and a higher charge transfer rate with increasing frequency as shown in Figure 5d. Figure 5e shows that the I_{SCSP3} and I_{SCDP3} values of the STENG and DTENG with the Al/Ti electrodes depend on bidirectional wind at 15.9 m s^{-1}.

The I_{SCSP3} values of the STENG decrease from 67 μA to 0 when the incident angle of wind direction increases 0° to 180°. Given that the I_{SCDP3} values of the DTENG decrease from 57 μA to 0 when the incident angle increases 0° to 90°, and then the I_{SCDP3} values increase from 0 to 55 μA when the incident angle increases 90° to 180°, indicating that bidirectional wind energy can be harvested by the DTENG. The I_{SCSP3} and I_{SCDP3} values are different by varying the incident angle ranging from 0° to 180°, inferring that bidirectional wind energy can be effectively harvested in 0° to 180° by the DTENG rather than that of the single-pathway-harvested STENG.[32,33] Figure 5f shows that the currents and output powers of the STENG and DTENG depend on external load ranging from 100 to 10^9 Ω, the I_{SR} and I_{DR} values of the STENG and DTENG gradually decrease from the I_{SC} values. The instantaneous powers of the P_{SR} and P_{DR} for the STENG and DTENG firstly increase and then decrease, which reach the maximum values of 5.5 and 3.4 mW at a matched load of 4 MΩ, respectively. The goal of the development of STENG and DTENG is to drive electronic devices by harvesting small-scale wind energy, so that the self-powered system can be realized.

To get a visualization of the DTENG powering external load, the DTENG is successfully demonstrated as a power source for simultaneously and continuously lighting up 118 commercial LEDs at wind speed of 3.7 m s^{-1}, as shown in **Figure 6**a,b (see Movie S2, Supporting Information). Figure 6c shows that the rectified I_{SC} values of the 1 × 1, 2 × 1, 2 × 2, and 4 × 1 STENG and DTENG arrays connected in parallel at wind velocity of 15.9 m s^{-1}, are assigned to the I_{SCSA1}, I_{SCDA1}, I_{SCSA2}, I_{SCDA2}, I_{SCSA3}, I_{SCDA3}, $I_{SCSA4,}$ and I_{SCDA4}, respectively, increasing visibly with the varied configurations of the STENG and DTENG arrays. The maximum values of the I_{SCSA4} and I_{SCDA4} for the 4 × 1 STENG and DTENG arrays reach 112 and 98 μA, respectively. Figure 6d shows frequencies of the F_{SSF} and F_{DSF} for the 1 × 1, 2 × 1, 2 × 2, and 4 × 1 STENG and DTENG arrays at wind velocity of 15.9 m s^{-1}, respectively. The F_{SSF} values of the STENG arrays increase from 173 to 275 Hz, while the F_{DSF} values of the DTENG arrays increase from 162 to 263 Hz. Compared to the I_{SCSA1}, I_{SCDA1}, I_{SCSA2}, I_{SCDA2}, I_{SCSA3}, I_{SCDA3}, I_{SCSA4}, and I_{SCDA4} values shown in Figure 6c, the I_{SC} values of the STENG arrays are larger than the counterparts of the DTENG arrays because F_{SSF} values are larger than those of the F_{DSF} values, resulting in more transferred charges, higher charge transfer rate and larger surface charge density for the corresponding STENG arrays.[11]

Figure 6e presents the comparison of durability and stability of the I_{SC} values for the 1 × 1, 2 × 1, 2 × 2, and 4 × 1 STENG and DTENG arrays at wind velocity of 15.9 m s^{-1}. When blowing time increases from 0 to 90 min, there is no degradation of the I_{SCS} and I_{SCD} values for the STENG and DTENG arrays. Furthermore, the I_{SCS} and I_{SCD} values of the 1 × 1, 2 × 1, 2 × 2, and 4 × 1 STENG and DTENG arrays decrease gradually with increasing the blowing time. Figure 6f shows the normalized I_{SCS} values for the STENG with the Al electrodes, the 1 × 1, 2 × 1, 2 × 2, and 4 × 1 STENG arrays with the Al/Ti electrodes, respectively. When the blowing time increases from 0 to 90 min, both the normalized $I_{SCS(1\times1)}$ with Al electrodes and the $I_{SCS(1\times1)}$ with Al/Ti electrodes are slightly degraded at wind velocity of 15.9 m s^{-1}. When the blowing time is 240 min at velocity of 15.9 m s^{-1}, the normalized I_{SCS} values of the 1 × 1 STENG with Al electrodes, 1 × 1, 2 × 1, 2 × 2, and 4 × 1 STENGs with Al/Ti electrodes are degraded by 69.8%, 40.3%, 13.3%, 12.4%, and 10.7%, respectively. Figure 6g shows the normalized I_{SCD} values for the DTENG with the Al electrodes, the 1 × 1, 2 × 1, 2 × 2, and 4 × 1 DTENG arrays with the Al/Ti electrodes, respectively. When the blowing time increases from 0 to 90 min, no degradation in the normalized $I_{SCD(1\times1)}$ with Al electrodes, the $I_{SCD(1\times1)}$, $I_{SCD(2\times1)}$, $I_{SCD(2\times2)}$, and $I_{SCD(4\times1)}$ with Al/Ti electrodes are observed at wind velocity of 15.9 m s^{-1}. Meanwhile, the normalized $I_{SCD(1\times1)}$ with Al electrodes, the $I_{SCD(1\times1)}$, $I_{SCD(2\times1)}$, $I_{SCD(2\times2)}$, and $I_{SCD(4\times1)}$ with Al/Ti electrodes are degraded by 48.7%, 8.8%, 7.9%, 4.5%, and 3.1%, respectively, when persistent time of wind blowing is 240 min. Therefore, durability and stability of the I_{SC} values for the DTENG arrays with Al/Ti electrodes can be significantly improved in comparison with the counterparts of the STENG arrays. The improved durability and stability is attributed to the device configuration and Ti buffer layers among Al, PTFE and Kapton thin films, configuring in the sandwiched PTFE/Ti/Al and Al/Ti/Kapton/Ti/Al thin films. By introducing Ti buffer layers, sticky, abrasive and triboelectric properties between the PTFE/Ti/Al and Al/Ti/Kapton/Ti/Al thin films are improved based on unique properties of Ti, including the sticky and electrical parameters: work function (4.33 eV), photoelectric threshold (4.59 eV), surface potential (173 mV), electronegativity (1.32), ionization energy (0.658 MJ mol^{-1}), electron affinity (20 kJ mol^{-1}) and electrical conductivity (0.23×10^7 S m^{-1})[31,34] (see the Supporting Information). As depicted in Figure 6h, we calculate the charging rates and error bars of a 10 μF capacitor charged by the rectified 1 × 1, 2 × 1, 2 × 2, and 4 × 1 STENG and DTENG arrays connected in parallel, respectively. The charging rates of both the STENG and DTENG arrays increase with the device configurations of the 1 × 1, 2 × 1, 2 × 2, and 4 × 1 arrays. Compared to the counterparts of the DTENG arrays, the rectified STENG arrays have better charging performances, especially for the 4 × 1 STENG array connected in parallel due to the higher fluttering frequency, resulting in the larger effective contact area, as presented in Figure 6d.

3. Conclusions

In summary, compared to the single-pathway-harvested STENG, the DTENG can harvest bidirectional wind energy with wind incident angles of 0° and 180°. The working mechanism is based on the coupling of triboelectrification and electrostatic induction between the PTFE/Ti/Al and the undulating Al/Ti/Kapton/Ti/Al thin film. Electric potential distributions of the STENG and DTENG at representative states are obtained by finite element method, while V_{OC} value of the DTENG is more stable than that of the STENG. The I_{SC}, V_{OC} and frequencies increase with increasing wind velocity in the range from 9.2 to 18.4 m s^{-1}, revealing that the corresponding values of the DTENG are 66 μA, 342 V at 178 Hz with wind speed of 18.4 m s^{-1}, respectively. The maximum output powers of the DTENG reach 3.4 mW at the matched load of 4 MΩ with wind velocity of 15.9 m s^{-1}. Compared with counterparts of the

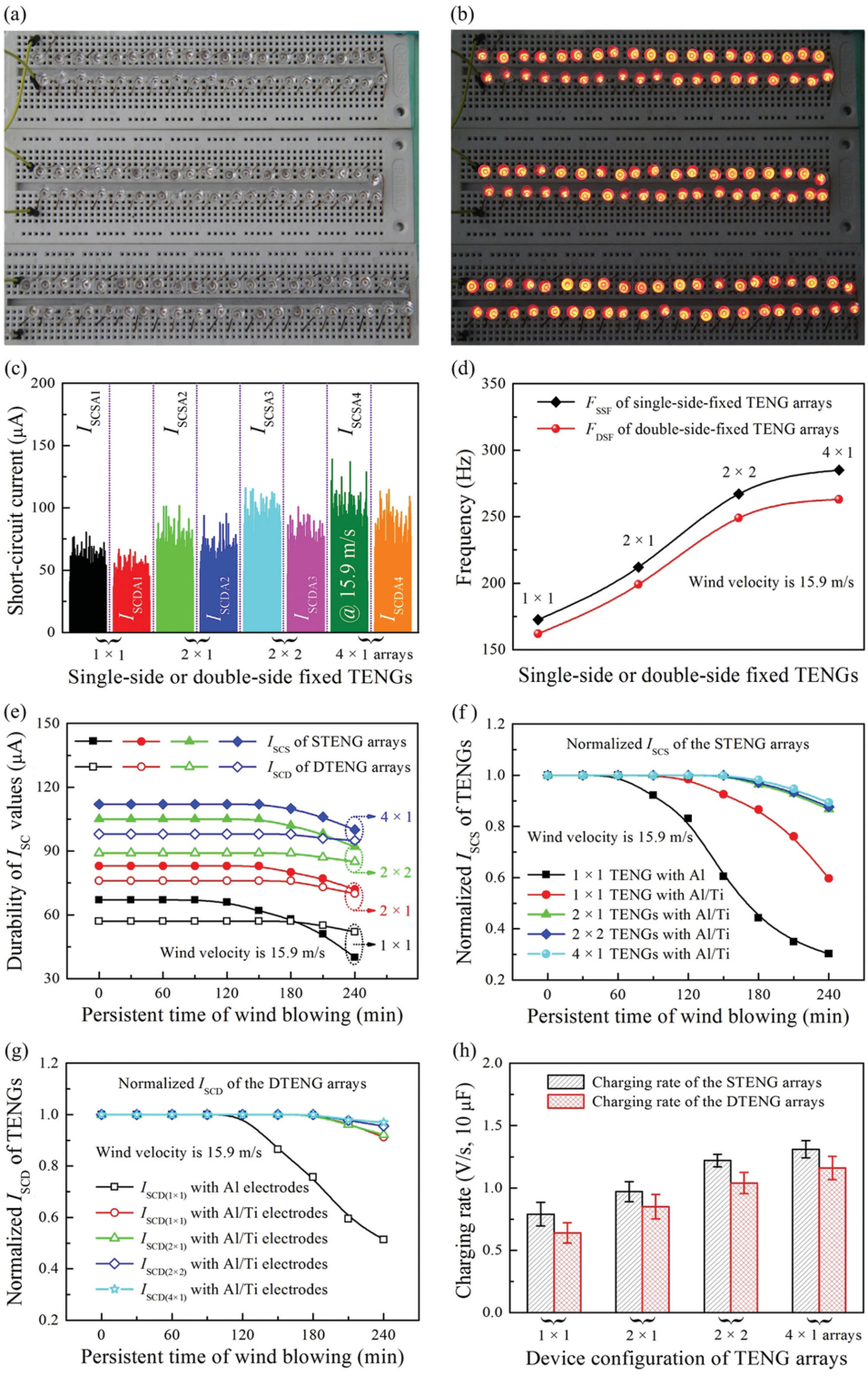

Figure 6. a,b) One hundred eighteen commercial LEDs before and after lighting by the DTENG with wind velocity ranging from 0 to 3.7 m s^{-1}. c) Rectified I_{SC} values of 1 × 1, 2 × 1, 2 × 2, and 4 × 1 STENG and DTENG at wind velocity of 15.9 m s^{-1}, respectively. d) Frequencies of the 1 × 1, 2 × 1, 2 × 2, and 4 × 1 STENG and DTENG arrays at wind velocity of 15.9 m s^{-1}. e) Durability of the 1 × 1, 2 × 1, 2 × 2, and 4 × 1 STENG and DTENG arrays at wind velocity of 15.9 m s^{-1}, respectively. Normalized I_{SC} values of f) the single-pathway-harvested STENG and g) the bidirectional-harvested DTENG depend on blowing time at velocity of 15.9 m s^{-1}. h) Charging rates and error bars of a 10 μF capacitor for the 1 × 1, 2 × 1, 2 × 2, and 4 × 1 STENG and DTENG arrays at wind velocity of 15.9 m s^{-1}, respectively.

single-pathway-harvested STENG arrays, the I_{SC}, durability and stability of the bidirectional-harvested DTENG can be dramatically improved by the 4×1 array connected in parallel according to synergetic roles of the improved device configuration, stickiness and abrasion by adhering Ti buffer layers. The stable and durable DTENG arrays present a step toward promising applications in harvesting bidirectional wind energy for self-powered systems and wireless sensors.

4. Experimental Section

Etching of PTFE Thin Films: PTFE thin films with thickness of 50 μm were first rinsed with alcohol, isopropyl alcohol, and deionized water, consecutively, and then blown dry by nitrogen. Subsequently, to improve triboelectric effects, PTFE thin films without any masks were etched by inductively coupled plasma (ICP, SI500, SENTECH Instruments Corp.). Etching details of PTFE thin films were listed in Table S1 (Supporting Information). Electrical performances of the STENG and DTENG could be improved by increasing total charge quantity, surface roughness, and effective surface area for the etched PTFE thin films.[13, 35, 36]

Fabrication of the STENG and DTENG Arrays: Both the STENG and DTENG consist of upper and lower PTFE/Ti/Al thin films and the middle Al/Ti/Kapton/Ti/Al thin film, where the sputtered Al/Ti bilayer electrodes were deposited on the Kapton and PTFE thin films, respectively. More sputtering parameters can be found in Table S2 (Supporting Information). The thickness and its error were evaluated by a Long Scan Profiler (P-7, KLA Tencor Corp.). An internal hollow acrylic tube with size of 70 mm × 20 mm × 10 mm was fabricated by a laser cutting machine (PLS6.75, Universal Laser Systems) to obtain four acrylic sheets, and more optimized details are described in Figures S1–S5 (Supporting Information). Sequential processes of contact separation between the upper and/or lower PTFE/Ti/Al and the middle Al/Ti/Kapton/Ti/Al films could be realized by airflow-driven vibration in the acrylic tube, resulting in the output electrical signals of the STENG and DTENG. Both the single STENG and DTENG have two TENGs (namely, TENG1 and TENG2 shown in Figure S1c, Supporting Information) in the acrylic tube. Several STENG and DTENG devices can be connected in parallel with 1×1, 2×1, 2×2, and 4×1 arrays by the rectified circuits (Supporting Information).

Numerical Simulation via COMSOL: 2D models of the STENG and DTENG with the size of 70 mm × 20 mm × 10 mm were built by COMSOL, which matched actual profiles of the undulate Al/Kapton/Al films at representative states (Supporting Information). Under an open-circuit (OC) condition, a surface charge density of -8×10^{-6} C m^{-2} was set for the top and bottom PTFE films, while the total charges of Al electrodes on both sides of Kapton were assigned to 1.12×10^{-8} C. The Al thin films on both sides of Kapton film have the same potential to reflect electric connection, as well as Al films on back sides of top and bottom PTFE films adhered on the acrylic tube.

Measurement of the STENG and DTENG Arrays: For measurements of the 1×1, 2×1, 2×2, and 4×1 STENG and DTENG arrays, wind was applied by a commercial air gun, and wind velocities were measured by a digital anemometer (Victor 816A, Shanghai Five Long Automation Equipment Co.). Output signals of both currents and capacitor-charging times for the STENG and DTENG arrays were measured by a system electrometer (6514, Keithley Instruments Inc.). Output voltages and frequencies of the STENG and DTENG arrays can be analyzed by the 6514 electrometer and a digital storage oscilloscope (InfiniiVision DSO-X 2014A, Agilent Technologies Co.).

Supporting Information

Supporting Information is available from the Wiley Online Library or from the author.

Acknowledgements

This research was supported by the "Thousands Talents" Program for Pioneer Researcher and His Innovation Team of People's Republic of China. Z.C.Q. gratefully acknowledges financial supports from the National Natural Science Foundation of China (Grant No. 11364032), 2015 Key Project of Jiangxi Provincial Education Department and China Postdoctoral Science Foundation (Grant No. 2014M560931). Patents have been filed based on the research results presented in this article. The authors declare no competing financial interest.

Received: September 9, 2015
Revised: October 22, 2015
Published online:

[1] X. D. Wang, J. H. Song, J. Liu, Z. L. Wang, *Science* **2007**, *316*, 102.
[2] M. L. Seol, J. H. Woo, S. B. Jeon, D. Kim, S. J. Park, J. Hur, Y. K. Choi, *Nano Energy* **2015**, *14*, 201.
[3] J. Bae, J. Lee, S. M. Kim, J. Ha, B. S. Lee, Y. Park, C. Choong, J. B. Kim, Z. L. Wang, H. Y. Kim, J. J. Park, U. I. Chung, *Nat. Commun.* **2014**, *5*, 4929.
[4] H. Y. Guo, X. M. He, J. W. Zhong, Q. Z. Zhong, Q. Leng, C. G. Hu, J. Chen, L. Tian, Y. Xi, J. Zhou, *J. Mater. Chem. A* **2014**, *2*, 2079.
[5] Z. L. Wang, *Faraday Discuss.* **2014**, *176*, 447.
[6] X. Pu, L. X. Li, H. Q. Song, C. H. Du, Z. F. Zhao, C. Y. Jiang, G. Z. Cao, W. G. Hu, Z. L. Wang, *Adv. Mater.* **2015**, *27*, 2472.
[7] C. Xu, C. F. Pan, Y. Liu, Z. L. Wang, *Nano Energy* **2012**, *1*, 259.
[8] Y. C. Wu, X. D. Zhong, X. Wang, Y. Yang, Z. L. Wang, *Nano Res.* **2014**, *7*, 1631.
[9] D. Kim, S. B. Jeon, J. Y. Kim, M. L. Seol, S. O. Kim, Y. K. Choi, *Nano Energy* **2015**, *12*, 331.
[10] X. Wang, S. H. Wang, Y. Yang, Z. L. Wang, *ACS Nano* **2015**, *9*, 4553.
[11] Z. L. Wang, *ACS Nano* **2013**, *7*, 9533.
[12] S. H. Wang, Y. N. Xie, S. M. Niu, L. Lin, Z. L. Wang, *Adv. Mater.* **2014**, *26*, 2818.
[13] G. Zhu, B. Peng, J. Chen, Q. S. Jing, Z. L. Wang, *Nano Energy* **2015**, *14*, 126.
[14] H. Y. Guo, Q. Leng, X. M. He, M. J. Wang, J. Chen, C. G. Hu, Y. Xi, *Adv. Energy Mater.* **2015**, *5*, 1400790.
[15] G. Zhu, Z. H. Lin, Q. S. Jing, P. Bai, C. F. Pan, Y. Yang, Y. S. Zhou, Z. L. Wang, *Nano Lett.* **2013**, *13*, 847.
[16] M. Kanik, M. G. Say, B. Daglar, A. F. Yavuz, M. H. Dolas, M. M. El-Ashry, M. Bayindir, *Adv. Mater.* **2015**, *27*, 2367.
[17] Y. N. Xie, S. H. Wang, L. Lin, Q. S. Jing, Z. H. Lin, S. M. Niu, Z. Y. Wu, Z. L. Wang, *ACS Nano* **2013**, *7*, 7119.
[18] Y. F. Hu, Z. L. Wang, *Nano Energy* **2015**, *14*, 3.
[19] Z. L. Wang, J. H. Song, *Science* **2006**, *312*, 242.
[20] Y. Qin, X. D. Wang, Z. L. Wang, *Nature* **2008**, *451*, 809.
[21] C. Zhang, L. M. Zhang, W. Tang, C. B. Han, Z. L. Wang, *Adv. Mater.* **2015**, *27*, 3533.
[22] W. Z. Wu, L. Wang, Y. L. Li, F. Zhang, L. Lin, S. M. Niu, D. Chenet, X. Zhang, Y. F. Hao, T. F. Heinz, J. Hone, Z. L. Wang, *Nature* **2014**, *514*, 470.
[23] Y. L. Zi, L. Lin, J. Wang, S. H. Wang, J. Chen, X. Fan, P. K. Yang, F. Yi, Z. L. Wang, *Adv. Mater.* **2015**, *27*, 2340.
[24] X. Chen, S. Y. Xu, N. Yao, Y. Shi, *Nano Lett.* **2010**, *10*, 2133.
[25] K. I. Park, S. Xu, Y. Liu, G. T. Hwang, S. J. L. Kang, Z. L. Wang, K. J. Lee, *Nano Lett.* **2010**, *10*, 4939.

[26] Z. C. Quan, W. Liu, H. Hu, S. Xu, B. Bebo, G. J. Fang, M. Y. Li, X. Z. Zhao, *J. Appl. Phys.* **2008**, *104*, 084106.
[27] Q. T. Xue, Z. Wang, H. Tian, Y. Huan, Q. Y. Xie, Y. Yang, D. Xie, C. Li, Y. Shu, X. H. Wang, T. L. Ren, *AIP Adv.* **2015**, *5*, 017102.
[28] J. M. Wu, X. Chen, Y. Zhang, Y. Yang, Y. S. Zhou, Z. L. Wang, *Adv. Mater.* **2012**, *24*, 6094.
[29] M. Argentina, L. Mahadevan, *Proc. Natl. Acad. Sci. USA* **2005**, *102*, 1829.
[30] X. S. Meng, G. Zhu, Z. L. Wang, *ACS Appl. Mater. Interfaces* **2014**, *6*, 8011.
[31] Y. Momose, Y. Yamashita, *Tribol. Int.* **2012**, *48*, 232.
[32] S. H. Wang, X. J. Mu, Y. Yang, C. L. Sun, A. Y. Gu, Z. L. Wang, *Adv. Mater.* **2015**, *27*, 240.
[33] Y. Yang, G. Zhu, H. L. Zhang, J. Chen, X. D. Zhong, Z. H. Lin, Y. J. Su, P. Bai, X. N. Wen, Z. L. Wang, *ACS Nano* **2013**, *7*, 9461.
[34] M. L. Seol, J. H. Woo, D. I. Lee, H. Im, J. Hur, Y. K. Choi, *Small* **2014**, *10*, 3887.
[35] Z. C. Quan, B. S. Zhang, T. J. Zhang, T. Guo, R. K. Pan, J. Jiang, *Microelectron. Eng.* **2007**, *84*, 631.
[36] Z. C. Quan, S. Xu, H. Hu, W. Liu, H. M. Huang, B. Sebo, G. J. Fang, M. Y. Li, X. Z. Zhao, *Microelectron. Eng.* **2008**, *85*, 2269.